Inorg. Chem. **XXXX**, *XX*,

Inorganic Chemistry
Article

Controlling Phosphorescence Color and Quantum Yields in Cationic Iridium Complexes: A Combined Experimental and Theoretical Study

Filippo De Angelis,*,† Simona Fantacci,† Nicholas Evans,‡ Cedric Klein,‡ Shaik M. Zakeeruddin,‡ Jacques-E. Moser,‡ Kuppuswamy Kalyanasundaram,‡ Henk J. Bolink,§ M. Grätzel,‡ and Mohammed K. Nazeeruddin*,‡

Istituto CNR di Scienze e Tecnologie Molecolari (ISTM-CNR), c/o Dipartimento di Chimica, Università di Perugia, Via elce di Sotto 8, I-06213, Perugia, Italy, Laboratory for Photonics and Interfaces, Station 6, Institute of Chemical Sciences and Engineering, School of basic Sciences, Swiss Federal Institute of Technology, CH - 1015 Lausanne, Switzerland, and Instituto de Ciencia Molecular, Universidid de Valencia, P.O. Box 22085, 46071 Valencia, Spain

Received March 6, 2007

We report a combined experimental and theoretical study on cationic Ir(III) complexes for OLED applications and describe a strategy to tune the phosphorescence wavelength and to enhance the emission quantum yields for this class of compounds. This is achieved by modulating the electronic structure and the excited states of the complexes by selective ligand functionalization. In particular, we report the synthesis, electrochemical characterization, and photophysical properties of a new cationic Ir(III) complex, [Ir(2,4-difluorophenylpyridine)$_2$(4,4′-dimethylamino-2,2′-bipyridine)](PF_6) (N969), and compare the results with those reported for the analogous [Ir(2-phenylpyridine)$_2$(4,4′-dimethylamino-2,2′-bipyridine)](PF_6) (N926) and for the prototype [Ir(2-phenylpyridine)$_2$(4,4′-*tert*-butyl-2,2′-bipyridine)]-(PF_6) complex, hereafter labeled N925. The three complexes allow us to explore the (C^N) and (N^N) ligand functionalization: considering N925 as a reference, we investigate in N926 the effect of electron-releasing substituents on the bipyridine ligand, while in N969, we investigate the combined effect of electron-releasing substituents on the bipyridine ligand and the effect of electron-withdrawing substituents on the phenylpyridine ligands. For N969 we obtain blue-green emission at 463 nm with unprecedented high quantum yield of 85% in acetonitrile solution at room temperature. To gain insight into the factors responsible for the emission color change and the different quantum yields, we perform DFT and TDDFT calculations on the ground and excited states of the three complexes, characterizing the excited-state geometries and including solvation effects on the calculation of the excited states. This computational procedure allows us to provide a detailed assignment of the excited states involved in the absorption and emission processes and to rationalize the factors determining the efficiency of radiative and nonradiative deactivation pathways in the investigated complexes. This work represents an example of electronic structure-driven tuning of the excited-state properties, thus opening the way to a combined theoretical and experimental strategy for the design of new iridium(III) phosphors with specific target characteristics.

Introduction

Iridium(III) cyclometalated complexes are attracting widespread interest because of their unique photophysical properties and applications in organic light-emitting diodes (OLEDs). Several groups have used extensively neutral iridium cyclometalated complexes in OLEDs and obtained up to 19% external quantum efficiencies; the use of neutral iridium complexes, however, requires a complicated multilayered structure for charge injection, transport, and light emission.[1−4] The *tris*-orthometalated iridium(III) complexes have been

* To whom correspondence should be addressed. E-Mail: filippo@thch.unipg.it (F.D.A.); MdKhaja.Nazeeruddin@epfl.ch (M.K.N.).
† ISTM-CNR Perugia.
‡ Swiss Federal Institute of Technology.
§ University of Valencia.

(1) Adachi, C.; Baldo, M. A.; Thompson, M. E.; Forrest, S. R. *J. Appl. Phys.* **2001**, *90*, 5048.
(2) Baldo, M. A.; Lamansky, S.; Burrows, P. E.; Thompson, M. E.; Forrest, S. R. *Appl. Phys. Lett.* **1999**, *75*, 4.
(3) Ikai, M.; Tokito, S.; Sakamoto, Y.; Suzuki, T.; Taga, Y. *Appl. Phys. Lett.* **2001**, *79*, 156.
(4) Nazeeruddin, M. K.; Humphry-Baker, R.; Berner, D.; Rivier, B. S.; Zuppiroli, L.; Grätzel, M. *J. Am. Chem. Soc.* **2003**, *125*, 8790.

10.1021/ic700435c CCC: $37.00

Published on Web 06/21/2007

successfully used for OLED applications because of their high triplet quantum yields, which are the result of several factors:[5,6] (a) iridium has large d-orbital splitting compared to other metals in the series; (b) the strong ligand field strength of phenyl anion ligand that increases the energy between t_{2g} and e_g orbitals leading to enhanced gap between the e_g and LUMO of the ligand; and (c) the close-lying $\pi-\pi^*$ and MLCT states together with the heavy atom effect that enhances the spin−orbit coupling, thus increasing the efficiency of radiative deactivation pathways.

An alternative to neutral *tris*-orthometalated complexes is represented by mixed ligand cationic iridium complexes, which have been recently employed to fabricate single-layer devices.[7] The main difference between neutral and cationic iridium complexes is the presence in the latter of mobile counterions, which drift under the influence of an applied electric field leading to accumulation of negative charge near one electrode. This creates high electric fields at the electrodes, thus enhancing electronic charge injection ultimately allowing for the use of a single-layer architecture operating at low voltages.[7] However, the mixed-ligand cationic iridium complexes show appreciably low quantum yields compared to the *tris*-orthometalated iridium complexes,[7−9] exceptions being represented by a recently reported blue-emitting [Ir(bis-(4′,6′-difluorophenyl)-pyrazolato)$_2$-(4,4′-*tert*-butyl-2,2′-bipyridine)](PF_6) complex,[10] showing a room-temperature solution photoluminescence quantum yield of 40%, and by a blue-green emitting [Ir(2-phenylpyridine)$_2$-(4,4′-dimethylamino-2,2′-bipyridine)](PF_6) complex, for which we recently reported a room-temperature solution photoluminescence quantum yield of 80%.[11]

An attractive alternate to the OLEDs is the light-emitting electrochemical cell (LEC),[7,12−15] which is particularly promising for large-area lighting applications. In these cells, the use of ionic complexes facilitates electronic charge injection into the light emitting film.[7,16,17] The main requirements for LEC are that the phosphorescent emitter should have sharp colors in the red, green, and blue regions and exhibit very high phosphorescence quantum yields. Tuning phosphorescence wavelength and enhancing phosphorescent quantum yields in these complexes in a predictable way is a daunting task, which of course is attractive for both fundamental research and practical applications.[4,8,18−21]

A strategy to tune the emission color in iridium(III) complexes relies on the selective HOMO stabilization or LUMO destabilization of the complex. Mixed ligand cationic iridium complexes of the type $[Ir(C\hat{}N)_2(N\hat{}N)]^+$, with (C^N) cyclometalating and (N^N) bipyridine-like ligands, are particularly appealing in this respect because the two type of ligands can be almost independently functionalized to obtain the desired color tuning.[11,20] In particular, electron-withdrawing substituents on the (C^N) ligands decrease the donation to the metal and therefore stabilize the metal-based HOMO. Electron-releasing substituents on the (N^N) ligand, lead, on the other hand to destabilization of the (N^N) ligand-based LUMO, ultimately leading to increased HOMO−LUMO gaps and emission energies. Much less clear are the factors which determine the emission quantum yields in mixed ligand cationic complexes and on which parameters to act to increase them. It is indeed generally assumed that emission quantum yields should increase with increasing emission energy because of the increase of the radiative rate constant and decrease of the nonradiative rate constants, which follow, respectively, the Einstein law of spontaneous emission[22] and the so-called energy gap law,[23] even though several exceptions to these rules for cationic iridium(III) complexes have been reported.[8,10,24]

In this study, we report a combined experimental and theoretical study on cationic Ir(III) complexes for OLED applications and describe a strategy to tune the phosphorescence wavelength and to enhance the emission quantum yields for this class of compounds. This is achieved by modulation of the electronic structure and the excited states of the complexes by selective ligand functionalization.

In particular, we describe the synthesis, electrochemical characterization, and photophysical properties of a new cationic Ir(III) complex, [Ir(2,4-difluorophenylpyridine)$_2$(4,4′-dimethylamino-2,2′-bipyridine)](PF_6) (N969), and compare the results with those reported[11] for the analogous [Ir(2-phenylpyridine)$_2$(4,4′-dimethylamino-2,2′-bipyridine)](PF_6) (N926) and for the prototype [Ir(2-phenylpyridine)$_2$(4,4′-*tert*-butyl-2,2′-bipyridine)](PF_6) complex, hereafter labeled N925.[7] The three complexes allow us to explore the (C^N) and (N^N) ligand functionalization: considering N925 as a

(5) Ohsawa, Y.; Sprouse, S.; King, K. A.; DeArmond, M. K.; Hanck, K. W.; Watts, R. J. *J. Phys. Chem.* **1987**, *91*, 1047.
(6) Garces, F. O.; King, K. A.; Watts, R. J. *Inorg. Chem.* **1988**, *27*, 3464.
(7) Slinker, J. D.; Gorodetsky, A. A.; Lowry, M. S.; Wang, J.; Parker, S.; Rohl, R.; Bernhard, S.; Malliaras, G. G. *J. Am. Chem. Soc.* **2004**, *126*, 2763.
(8) Yang, C.-H.; Li, S.-W.; Chi, Y.; Cheng, Y.-M.; Yeh, Y.-S.; Chou, P.-T.; Lee, G.-H.; Wang, C. H.; Shu, C. F. *Inorg. Chem.* **2005**, *44*, 7770.
(9) King, K. A.; Watts, R. J. *J. Am. Chem. Soc.* **1987**, *109*, 1589.
(10) Tamayo, A. B.; Garon, S.; Sajoto, T.; Djurovich, P. I.; Tsyba, I. M.; Bau, R.; Thompson, M. E. *Inorg. Chem.* **2005**, *44*, 8723.
(11) Nazeeruddin, M. K.; Wegh, R. T.; Zhou, Z.; Klein, C.; Wang, A.; De Angelis, F.; Fantacci, S.; Grätzel, M. *Inorg. Chem.* **2006**, *45*, 9254.
(12) Slinker, J.; Bernards, D.; Houston, P. L.; Abruna, H. D.; Bernhard, S.; Malliaras, G. G. *Chem. Commun.* **2003**, 2392.
(13) Rudmann, H.; Shimida, S.; Rubner, M. F. *J. Am. Chem. Soc.* **2002**, *124*, 4918.
(14) Bernhard, S.; Barron, J. A.; Houston, P. L.; Abruna, H. D.; Ruglovksy, J. L.; Gao, X.; Malliaras, G. G. *J. Am. Chem. Soc.* **2002**, *124*, 13624.
(15) Wegh, R. T.; Meijer, E. J.; Plummer, E. A.; De Cola, L.; Brunner, K.; van Dijken, A.; Hofstraat, J. W. *Proc. SPIE−Int. Soc. Opt. Eng.* **2004**, *5519*, 48.
(16) Handy, E. S.; Pal, A. J.; Rubner, M. F. *J. Am. Chem. Soc.* **1999**, *121*, 3525.
(17) Gao, F. G.; Bard, A. J. *J. Am. Chem. Soc.* **2000**, *122*, 7426.
(18) Coppo, P.; Plummer, E. A.; De Cola, L. *Chem. Commun.* **2004**, 1774.
(19) Sajoto, T.; Djurovich, P. I.; Tamayo, A.; Yousufuddin, M.; Bau, R.; Thompson, M. E.; Holmes, R. H.; Forrest, S. R. *Inorg. Chem.* **2005**, *44*, 7992.
(20) (a) Lowry, M. S.; Hudson, W. R.; Pascal, R. A., Jr.; Bernhard, S. *J. Am. Chem. Soc.* **2004**, *126*, 14129. (b) Lowry, M. S.; Bernhard, S. *Chem.−Eur. J.* **2006**, *12*, 7970.
(21) You, Y.; Park, S. Y. *J. Am. Chem. Soc.* **2005**, *127*, 12438.
(22) (a) Strickler, S. J.; Berg, R. A. *J. Chem. Phys.* **1962**, *37*, 814. (b) Einstein, A. *Physik. Z.* **1917**, *18*, 121.
(23) (a) Kober, E. M.; Caspar, J. V.; Lumpkin, R. S.; Meyer, T. J. *J. Phys. Chem.* **1986**, *90*, 3722. (b) Henry, B. R.; Siebrand, W. In *Organic Molecular Photophysics*; Birks, J. B., Ed.; Wiley, New York, 1973; Vol. 1, Chapter 4. (c) Freed, K. F.; Jortner, J. *J. Chem. Phys.* **1970**, *52*, 6272. (d) Bixon, M.; Jortner, J. *J. Chem. Phys.* **1968**, *48*, 715.
(24) Lo, S. C.; Shipley, C. P.; Bera, R. N.; Harding, R. E.; Cowley, A. R.; Burn, P. L.; Samuel, I. D. W. *Chem. Mater.* **2006**, *18*, 5119.

Scheme 1. Structure of the N969, N926, and N925 Iridium Complexes

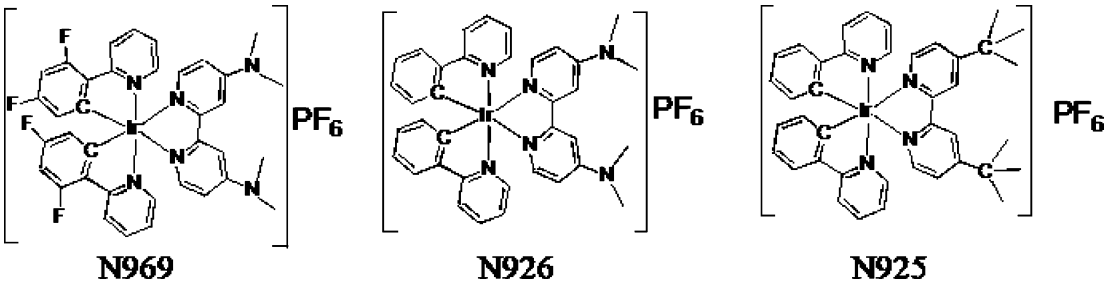

N969 N926 N925

reference, we investigate in N926 the effect of electron-releasing substituents on the bipyridine ligand, while in N969, we investigate the combined effect of electron-releasing substituents on the bipyridine ligand and the effect of electron-withdrawing substituents on the phenylpyridine ligands.

To gain insight into the factors responsible for the emission color change and for the different quantum yields, we perform density functional theory (DFT) and time-dependent DFT (TDDFT) calculations on the ground and excited states of the three complexes, characterizing the excited-state geometries and including solvation effects on the calculation of the excited states. This computational procedure allows us to provide a detailed assignment of the excited states involved in the absorption and emission processes and to rationalize the factors determining the efficiency of radiative and nonradiative deactivation pathways in the investigated complexes. Ground-state DFT calculations have become increasingly popular in conjunction to experimental electrochemical measurements to assign the character of the redox processes involving iridium(III) compounds,[10,11,20,21,24−32] by looking at the HOMO and LUMO localization. Information about the HOMO and LUMO is also often used to estimate the nature of the lowest excited states, assuming a single-orbital picture of the electronic transitions. In contrast to the ground-state DFT calculations, TDDFT excited-state calculations on iridium(III) complexes are scarce,[8,33−37] the first paper in the subject being the work by Hay[33] on the neutral [Ir(ppy)$_3$] complex, and the literature in this field is generally less developed than for the analogous d^6 ruthenium(II) compounds.[38] While TDDFT is more computationally demanding than ground-state DFT calculations, it provides in principle a more accurate description of the excitation energies and excited states than a one-particle approximation, since within TDDFT, the description of the excited states is based on a linear combination of single occupied-to-virtual orbital excitations, therefore providing information beyond a simple HOMO−LUMO picture. As we shall demonstrate in the following, this has a profound impact on the excited-state characterization of the investigated species.

Results and Discussion

Synthesis, Electrochemistry, and Photophysical Properties. The mixed-ligand complexes (see Scheme 1), [Ir(2,4-difluorophenylpyridine)$_2$(4,4′-dimethylamino-2,2′-bipyridine)](PF$_6$) (N969) and [Ir(2-phenylpyridine)$_2$(4,4′-dimethylamino-2,2′-bipyridine)](PF$_6$) (N926), were synthesized in a low boiling solvent dichloromethane by reaction of the corresponding dichloro-bridged iridium(III) dimer with 4,4′-bis-(dimethylamino)-2,2′-bipyridine ligand, and they were characterized by analytical and spectroscopic techniques.

The cyclic voltammogram of the N969 complex measured in acetonitrile containing 0.1 M tetrabutylammonium hexafluorophosphate with 100 mV/s scan rate shows a reversible couple at 1.0 V vs Ferrocene (Fc) from the Ir(III) to Ir(IV) oxidation. The three reversible reduction waves at −2.13, −2.49, and −2.77 V vs Fc are assigned to the reduction of 4,4′-bis(dimethylamino)-2,2′-bipyridine and 2-(2,4-difluorophenyl)pyridine ligand, respectively. Under the same

(25) Dedeian, K.; Shi, J.; Shepherd, N.; Forsythe, E.; Morton, D. C. *Inorg. Chem.* **2005**, *44*, 4445.
(26) Zhao, Q.; Liu, S.; Wang, C.; Yu, M.; Li, L.; Li, F.; Yi, T.; Huang, C. *Inorg. Chem.* **2006**, *45*, 6152.
(27) Nozaki, K.; Takamori, K.; Nakatsugawa, Y.; Ohno, T. *Inorg. Chem.* **2006**, *45*, 6161.
(28) Bolink, H. J.; Cappelli, L.; Coronado, E.; Grätzel, M.; Orti, E.; Costa, R. D.; Viruela, P. M.; Nazeeruddin, M. K. *J. Am. Chem. Soc.* **2006**, *128*, 14786.
(29) Wilkinson, A. J.; Goeta, A. E.; Foster, C. E.; Williams, J. A. G. *Inorg. Chem.* **2004**, *43*, 6513.
(30) Kwon, T. H.; Cho, H. S.; Kim, M. K.; Kim, J. W.; Kim, J. J.; Lee, K. H.; Park, S. J.; Shin, I. S.; Kim, H.; Shin, D. M.; Chung, Y. K.; Hong, J. I. *Organometallics* **2006**, *24*, 1578.
(31) Lowry, M. S.; Goldsmith, J. I.; Slinker, J. D.; Rohl, R.; Pascal, R. A., Jr.; Maillaras, G. G.; Bernhard, S. *Chem. Mater.* **2005**, *17*, 5712.
(32) Wilkinson, A. J.; Puschmann, H.; Howard, J. A. K.; Foster, C. E.; Williams, J. A. G. *Inorg. Chem.* **2006**, *45*, 8685.
(33) Hay, P. J. *J. Phys. Chem. A* **2002**, *106*, 1634.
(34) Polson, M.; Ravaglia, M.; Fracasso, S.; Garavelli, M.; Scandola, F. *Inorg. Chem.* **2005**, *44*, 1282.
(35) Yang, C. H.; Su, W. L.; Fang, K. H.; Wang, S. P.; Sun, I. W. *Organometallics* **2006**, *25*, 4514.
(36) Polson, M.; Fracasso, S.; Bertolasi, V.; Ravaglia, M.; Scandola, F. *Inorg. Chem.* **2004**, *43*, 1950.
(37) Obara, S.; Itabashi, M.; Okuda, F.; Tamaki, S.; Tanabe, Y.; Ishii, Y.; Nozaki, K.; Haga, M.-a. *Inorg. Chem.* **2006**, *45*, 8907.
(38) (a) Monat, J. E.; Rodriguez, J. H.; McCusker, J. K. *J. Phys. Chem. A* **2002**, *106*, 7399. (b) Guillemoles, J.-F.; Barone, V.; Joubert, L.; Adamo, C. *J. Phys. Chem. A* **2002**, *106*, 11354. (c) Fantacci, S.; De Angelis, F. Selloni, A. *J. Am. Chem. Soc.* **2003**, *125*, 4381. (d) Zabri, H.; Gillaizeau, I.; Bignozzi, C. A.; Caramori, S.; Charlot, M.-F.; Cano-Boquera, J.; Odobel, F. *Inorg. Chem.* **2003**, *42*, 6655. (e) De Angelis, F.; Fantacci, S.; Selloni, A. *Chem. Phys. Lett.* **2004**, *389*, 204. (f) Fantacci, S.; De Angelis, F.; Wang, J.; Bernhard, S.; Selloni, A. *J. Am. Chem. Soc.* **2004**, *126*, 9715. (g) Ciofini, I.; Laine, P. P.; Bedioui, F.; Adamo, C. *J. Am. Chem. Soc.* **2004**, *126*, 10763. (h) Fantacci, S.; De Angelis, F.; Sgamellotti, A.; Re, N. *Chem. Phys. Lett.* **2004**, *396*, 43. (i) De Angelis, F.; Fantacci, S.; Selloni, A.; Nazeeruddin, M. K. *Chem. Phys. Lett.* **2005**, *415*, 115. (j) Fantacci, S.; De Angelis, F.; Sgamellotti, A.; Marrone, A.; Re, N. *J. Am. Chem. Soc.* **2005**, *127*, 14144. (k) Nazeeruddin, M. K.; De Angelis, F.; Fantacci, S.; Selloni, A.; Viscardi, G.; Liska, P.; Ito, S.; Takeru, B.; Grätzel, M. *J. Am. Chem. Soc.* **2005**, *127*, 16835. (l) Barolo, C.; Nazeeruddin, M. K.; Fantacci, S.; Di Censo, D.; Comte, P.; Liska, P.; Viscardi, G.; Quagliotto, P.; De Angelis, F.; Ito, S. Grätzel, M. *Inorg. Chem.* **2006**, *45*, 4642.

Table 1. Absorption, Emission, Lifetime, and Electrochemical Properties of the N925, N926, and N969 Iridium Cationic Complexes Measured in Acetonitrile

complex	absorption λ (nm) [ϵ ($\times 10^4$ M^{-1} cm^{-1})]	emission[a] λ (nm)	electrochemical data (V vs Fc)[b] $E_{ox}^{1/2}$	$E_{red}^{1/2}$	lifetime (μs)[c]	emission Φ_f	k_r ($\times 10^5$ s^{-1})	k_{nr} ($\times 10^5$ s^{-1})
N969	266 (8.27) 316 (2.89) 345 (2.20) 444 (0.14)	463 493	1.00	−2.13 −2.49 −2.77	4.11 ± 0.02	0.85 ± 0.1	2.07	0.40
N926	268 (5.62) 290 (3.49) 355 (0.95) 472 (0.19)	491 520	0.72	−2.17 −2.61 −2.87	2.43 ± 0.02	0.80 ± 0.1	3.29	0.80
N925[d]		581	0.83	−1.88	0.557	0.23	4.31	13.6

[a] Emission data were collected at 298 K by exciting at 380 nm. [b] Electrochemical potentials are in V vs Fc. [c] Lifetime data are collected in degassed acetonitrile solution. [d] Data measured in acetonitrile, taken from ref 5.

conditions, the cyclic voltammogram of the N926 complex[11] showed a reversible oxidation wave at 0.72 V vs Fc resulting from the Ir(III) to Ir(IV) oxidation and three reversible reduction waves at −2.17 and −2.61 and −2.87 V vs Fc, assigned to the reduction of 4,4′-dimethylamino-2,2′-bipyridine and the two 2-phenylpyridine ligands, respectively (Table 1).

It is interesting to note that the ligand-based reduction potentials of N969 and N926 are significantly shifted cathodically (by 0.250 and 0.290 V) compared to the N925 complex,[7] demonstrating that the destabilization of LUMO orbitals of the 4,4′-bis(dimethylamino)-2,2′-bipyridine ligand more than offsets the destabilization of iridium HOMO orbitals caused by the increased donor capability of the 4,4′-bis(dimethylamino)-2,2′-bipyridine compared to the 4,4′-*tert*-butyl-2,2′-bipyridine ligand. At the same time, the HOMO of N969 is stabilized by 0.280 V upon insertion of fluoride substituents on the phenyl pyridine ligands compared to N926, thus ensuring an increase in the gap between HOMO and LUMO of N969 compared to the N926 and N925 complexes[7] (see also the computational results).

UV−vis absorption spectra of the N969 and N926 complexes measured in acetonitrile solution at 298K display bands in the UV and the visible region resulting from intraligand ($\pi-\pi^*$) and metal-to-ligand charge-transfer transitions (MLCT), respectively (Figure 1 and Table 1).[39] When excited in acetonitrile solution at 298 K within the $\pi-\pi^*$ and MLCT absorption bands, the N969 complex shows emission maxima at 463 and 493 nm to be compared to emission maxima of 491 and 520 nm for N926 and 581 nm for N925, resulting in a considerable blue shift of the emission compared to the parent N925 and [Ir(2-phenylpyridine)$_2$(2,2′-bipyridine)]PF_6 complexes.[7,9]

It is worth noting that the argon-degassed acetonitrile solutions of N969 and N926 show bright luminescence in a lighted room and display remarkably high phosphorescence quantum yields of 80 and 85 ± 10%, respectively, at room temperature (see inset of Figure 1). The emission spectral profile is independent of excitation wavelength, and the

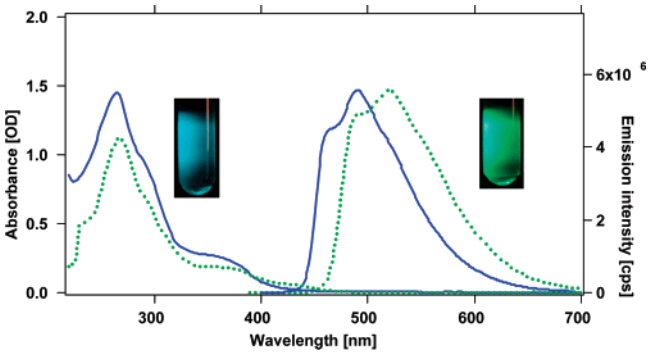

Figure 1. Absorption and emission spectra of [Ir(2,4-difluorophenylpyridine)$_2$(4,4′-dimethylamino-2,2′-bipyridine)](PF_6) (blue solid line, N969) and [Ir(2-phenylpyridine)$_2$(4,4′-dimethylamino-2,2′-bipyridine)](PF_6) (green dashed line, N926) in acetonitrile solution at 298 K. The inset shows a photo of the N969 and N926 solution exhibiting very strong blue-green and green emission, respectively, upon excitation at 380 nm.

emission decayed with lifetimes of 4.11 and 2.43 μs for N969 and N926, respectively, in CH_3CN solution.[40] The observed lifetimes are consistent with emission from a triplet state. This is confirmed by the substantial decrease in lifetime of aerated solution of the two complexes (0.265 and 0.042 μs for N969 and N926, respectively) compared to argon-degassed solutions. The shorter lifetime in aerated solution is caused by quenching of the intense emission from the triplet excited state to the ground state by triplet oxygen because of triplet−triplet energy transfer. A factor of 58 for the N926 complex clearly reveals its potential use as oxygen sensor.[41,42] By monitoring the excited-state decay dynamics, we found that the energy transfer from the initially excited high-energy intraligand ($\pi-\pi^*$) and metal-to-ligand charge-transfer states to the emitting triplet state takes place in less than 25 ns. The most probable mechanism is that after excitation to the singlet manifold of excited states, efficient intersystem crossing to the triplet manifold occurs because of the strong spin−orbit coupling of the iridium center. For N926 and N969, emission spectra at 77 K in iPrOH glasses

(39) Schmid, B.; Garces, F. O.; Watts, R. J. *Inorg. Chem.* **1994**, *33*, 9.

(40) Ichimura, K.; Kobayashi, T.; King, K. A.; Watts, R. J. *J. Phys. Chem.* **1987**, *91*, 6104.

(41) Köse, M. E.; Crutchley, R. J.; DeRosa, M. C.; Ananthakrishnan, N.; Reynolds, J. R.; Schanze, K. S. *Langmuir* **2005**, *21*, 8255.

(42) DeRosa, M. C.; Hodgson, D. J.; Enright, G. D.; Dawson, B.; Evans, C. E. B.; Crutchley, R. J. *J. Am. Chem. Soc.* **2004**, *126*, 7619.

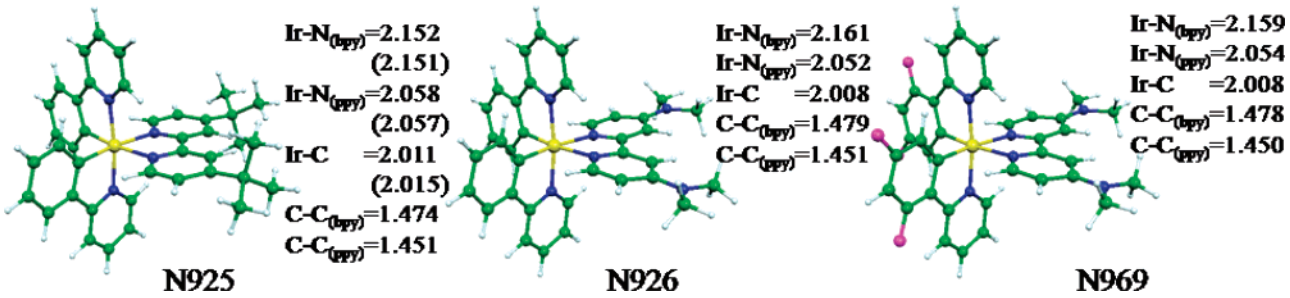

Figure 2. Optimized molecular structures and main calculated geometrical parameters for N925, N926, and N969. For N925, available X-ray data from ref 45 for the related $[Ir(2\text{-phenylpyridine})_2(4,4'\text{-}C_9H_{19}\text{-}2,2'\text{-bipyridine})]^+$ complex are reported in parenthesis.

were also recorded (see Supporting Information). Compared to the room-temperature emission spectra, the ones obtained at 77 K display a better resolution of the vibronic substructure but only a slight blue-shift of the main emission features. As an example, for N969 (N926), the high-energy emission features shifts from 463 (491) to 457 (479) nm. A summary of spectroscopic and electrochemical data for N925−N969 is presented in Table 1.

Comparison of the photophysical properties of the N926 and N969 species with those previously reported for the N925 complex shows that the N926 and N969 complexes have increased phosphorescence quantum yields and lifetimes and their spectra show a well-resolved vibronic structure at room-temperature, both factors being suggestive of increased ligand character in the emitting state.[43,44] From the phosphorescence quantum yields and lifetimes, assuming a unitary intersystem crossing quantum yield, it is possible to calculate the radiative (k_r) and nonradiative (k_{nr}) decay rates, which are reported in Table 1. As can be noticed, on going from N925 to N926 and N969, the radiative rate constant decreases by approximately a factor 2; at the same time, however, the nonradiative rate constant decreases by a factor of ∼34, so that the increased quantum yields of N926 and N969 compared to N925 are essentially the result of the diminished rate of nonradiative processes. While the decreased k_{nr} values with increasing emission energy are in line with the behavior predicted by the energy-gap law, the decrease in k_r suggests a partial change of the character of the emitting transition on going from N925 to N926 and N969. A detailed assignment of the nature of the excited states involved in the absorption and emission processes is given below, on theoretical grounds.

Geometry and Electronic Structure. Geometry optimization of the singlet ground state (S_0) of the investigated complexes led to similar structures for N925, N926, and N969. The main optimized geometrical parameters are reported in Figure 2, a detailed list of optimized parameters can be found in the Supporting Information. The calculated structures are in excellent agreement with experimental data for the complex $[Ir(2\text{-phenylpyridine})_2(4,4'\text{-}C_9H_{19}\text{-}2,2'\text{-bipyridine})]^+$, for which X-ray data are available.[45] Ir−N and Ir−C distances in the range of 2.15−2.16 (bipyridine), 2.05−2.06 (phenylpyridine), and 2.01 Å are calculated, to be compared to experimental values of 2.15, 2.06, and 2.02 Å, respectively. Most notably, bond angles are reproduced to the same degree of accuracy as bond lengths, see Supporting Information. The good agreement between calculated and experimental data highlights the importance of relativistic effects for a proper description of the geometrical structure of the present Ir(III) complexes.

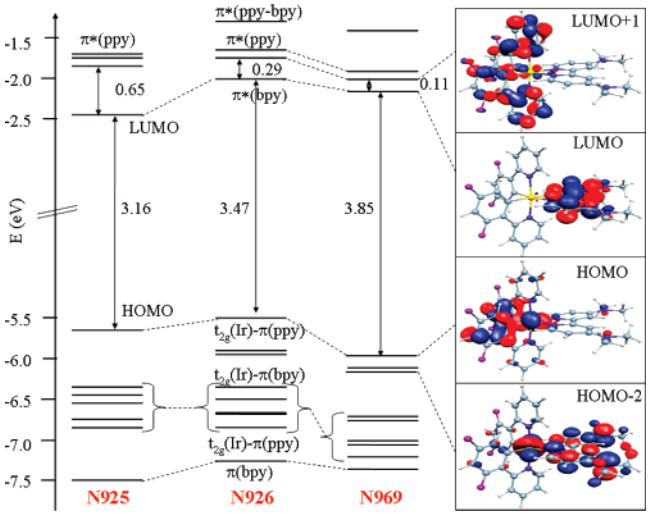

Figure 3. Calculated electronic structure in acetonitrile solution for the N925, N926, and N969 complexes at their S_0 optimized geometries. Also shown are isodensity surface plots of selected molecular orbitals of the N 969 complex.

To provide insight into the electronic structure of the N925, N926, and N969 complexes, we report in Figure 3 the results of single-point calculations performed at the S_0-optimized geometries in acetonitrile solution, which is the solvent used for the data in Table 1, together with plots of selected molecular orbitals for N969. We discuss here Kohn−Sham molecular orbital energies and their spatial localization in analogy to their Hartree−Fock counterparts, for which the negative of the energy of the highest-occupied molecular orbital (HOMO) and of the lowest-unoccupied molecular orbital (LUMO) represent, respectively, estimates of the ionization potential and electron affinity of the system. Moreover, we notice that a comparison of the calculated HOMO−LUMO gaps with the corresponding quantities measured by electrochemical studies is not straightforward because the calculated values are approximations to vertical oxidation/reduction potentials, while the electrochemical

(43) Colombo, M. G.; Hauser, A.; Güdel, H. U. *Inorg. Chem.* **1993**, *32*, 3088.
(44) Colombo, M. G.; Brunold, T. C.; Riedener, T.; Güdel, H. U.; Förtsch, M.; Bürgi, H.-B. *Inorg. Chem.* **1994**, *33*, 545.
(45) Neve, F.; La Deda, M.; Crispini, A.; Bellusci, A.; Puntoriero, F.; Campagna, S. *Organometallics* **2004**, *23*, 5856.

potentials refer to adiabatic processes, in which both the oxidized and reduced species are at their equilibrium geometries.

The electronic structure of the three complexes is rather similar, although sizable differences between the N926/N969 and the N925 complexes are found. The HOMO of the three complexes is an antibonding combination of Ir(t_{2g}; d_{xy}) and ppy(π) orbitals of A symmetry, see Figure 3, and is calculated at −5.66, −5.50, and −5.99 eV for N925, N926, and N969, respectively. The HOMO of N969 is stabilized compared to those of N926 and N925 because of the presence of fluoride substituents on the phenyl ring, which act as electron acceptors. The contribution of Ir orbitals to the HOMO ranges from 44.8% in N925 to 46.8 and 44.4% in N926 and N969, respectively. For N926 and N969, the HOMO is followed, in order of decreasing energy, by two almost degenerate combinations of Ir(t_{2g}; $d_{xz}-d_{yz}$) and π orbitals of the 4,4′-bis(dimethylamino)-2,2′-bipyridine ligand, which are missing in the N925 complex and have a metal contribution of 40.7−37.9 and 22.8−30.3% in N926 and N969, respectively. The HOMO−1 is calculated to lie 0.49 and 0.20 eV below the HOMO for N926 and N969, respectively; the strong stabilization of the Ir(t_{2g}; d_{xy})−ppy(π) HOMO in N969 only partially reflects on the energies of the Ir(t_{2g}; $d_{xz}-d_{yz}$)−bpy(π) HOMO−1/HOMO−2, so that the gap between the HOMO and the HOMO−1/HOMO−2 couple effectively decreases in N969 compared to that of N926. Still at lower energy, five combinations of Ir(t_{2g}) and ppy(π) orbitals, with decreasing percentage of metal character, are found, which are followed by the π-bonding framework of the 4,4′-substituted 2,2′-bipyridine. The LUMO of the three complexes is a π^* orbital of B symmetry localized on the substituted bipyridine ligand and is calculated to lie at −2.49, −2.03, and −2.14 eV for N925, N926, and N969 respectively. At higher energy, the LUMO is followed by an almost degenerate couple of (substituted) ppy π^* orbitals of A and B symmetry, respectively, whose energy approaches that of the substituted bipyridine π^* LUMO on going from N925 to N926 and N969. The HOMO−LUMO gaps increase substantially on going from N925 to N926 and N969, reflecting the HOMOs and LUMOs stabilization and destabilization, respectively, taking place in N926 and N969 compared to that in N925. Our calculated electronic structure is fully consistent with experimental electrochemical data, showing an increase of oxidation and reduction potentials of 110 (290) mV, respectively, on going from the N925 to the N926 complex and an increase (decrease) of the oxidation (reduction) potential of 280 (40) mV, respectively, on going from N926 to N969. We also notice that Ir orbitals which would belong to the e_g representation in octahedral symmetry (i.e., d_{z^2} and $d_{x^2-y^2}$) lie at much higher energy, being, for N926, the LUMO+12/LUMO+14 and the LUMO+15, calculated to lie 3.00/3.21 and 3.66 eV above the LUMO, respectively, and for N969 the LUMO+12 and LUMO+13, calculated to lie 2.77 and 2.78 eV above the LUMO, respectively.

Starting from the optimized S_0 geometries and imposing a triplet spin multiplicity, we selectively populated the bpy-based π^* LUMO of B symmetry (T_1) and the ppy-based LUMO+2 of A symmetry (T_2). We populate the LUMO+2 rather than the LUMO+1 of B symmetry since population of the latter would lead to collapse of this state to that obtained by population of the LUMO having the same B symmetry. Given the spatial and energy degeneracy of the LUMO+1/LUMO+2, we expect population of the LUMO+1 or LUMO+2 to lead to essentially the same results. Selected optimized geometrical parameters for the T_1 and T_2 states of the three complexes are reported in Supporting Information. In all cases, T_1 lies at lower energy than T_2. The geometrical variations observed for the triplet states mainly involve the bridging C−C bond of the bpy and ppy ligands (in T_1 and T_2, respectively) and to a minor extent the Ir−$N_{(bpy)}$ and Ir−C distances, suggesting that the investigated ligands form a rigid scaffold around the metal center with strong metal−ligand interactions. We also point out that the singlet ground state electronic structure calculated at the T_1 and T_2 geometries show the same orbital pattern calculated for the S_0 geometry, even though sizable changes in the orbital energies take place; in particular, at the T_1 (T_2) geometries, the bpy (ppy) π^* LUMOs are stabilized compared to the S_0 geometry.

For all the investigated species, a considerable shortening of the C−$C_{(bpy)}$ distance is observed in T_1 compared to that in S_0, while in T_2, this parameter remains essentially unchanged, see Supporting Information. On the other hand, in T_2, the C−$C_{(ppy)}$ bond is shortened, while the C−$C_{(bpy)}$ bond is unchanged. These geometrical trends are in line with the electronic structure discussed above: the LUMO, localized within the bpy ligand, is bonding with respect to the C−$C_{(bpy)}$ bond, while the LUMO+1/LUMO+2, localized within the ppy ligands, are bonding with respect to the C−$C_{(ppy)}$ bond. By looking at the metal−ligand bonds, we notice that for N926 and N969 a slight contraction (lengthening) of the Ir−$N_{(bpy)}$ distance is observed in T_1 (T_2) compared to S_0 (−0.014/0.026 and −0.16/0.17 Å for N926 and N969, respectively), while for N925 a slight increase of this parameter is observed for both triplet states. For all the investigated species, Ir−C distances are found to remain almost constant in T_1, while they are calculated to decrease by 0.025−0.026 Å on going from S_0 to T_2. Thus, we find that population of the bpy-based π^* orbitals leads to shortening of the Ir−$N_{(bpy)}$ distances, while the Ir−$N_{(ppy)}$ and Ir−C distances are unaffected; population of the ppy-based π^* orbitals leads, on the other hand, to shortening (lengthening) of the Ir−C (Ir−$N_{(bpy)}$) distances, while the Ir−$N_{(ppy)}$ bonds are almost unaffected. Since one electron is promoted from the same HOMO to different LUMOs, this geometrical variation can be rationalized in terms of the character of the π^* orbitals which are being populated in T_1 and T_2. Basically, population of antibonding orbitals of the bpy or ppy ligands weakens the bonding interactions within that ligand and increases the electron density available for donation to the metal, thus increasing the metal−ligand bond strength. However, while the strong Ir−C bonds are merely affected by slight variations of the Ir−$N_{(bpy)}$ bonds trans to the Ir−C bonds, as is the case in T_1, the more consistent decrease of

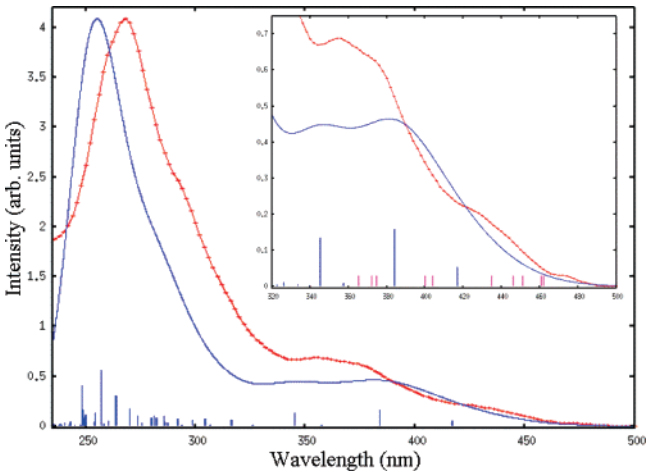

Figure 4. Comparison of the calculated (blue line) and experimental (red line) absorption spectra of N926 in acetonitrile solution. Blue vertical lines correspond to unbroadened oscillator strength of calculated singlet−singlet transitions. The insert shows a detail of the low-energy spectra region, with both singlet−singlet (blue vertical lines) and singlet−triplet calculated transitions (magenta vertical lines), the latter with arbitrary intensity to indicate their positions.

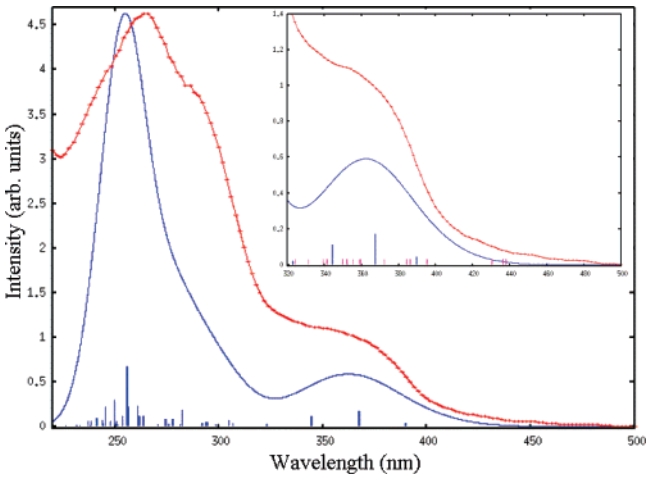

Figure 5. Comparison of the calculated (blue line) and experimental (red line) absorption spectra of N969 in CH_2Cl_2 solution. Blue vertical lines correspond to unbroadened oscillator strength of calculated singlet−singlet transitions. The insert shows a detail of the low-energy spectra region, with both singlet−singlet (blue vertical lines) and singlet−triplet calculated transitions (magenta vertical lines), the latter with arbitrary intensity to indicate their positions.

the Ir−C bonds in T_2 leads to lengthening of the Ir−$N_{(bpy)}$ bonds trans to the Ir−C bonds. We finally remark that for N926 the geometrical variations observed on going from S_0 to T_1 are essentially the same, considering an SCF or TDDFT optimized geometry for the lowest triplet excited state, see Computational Details. In the TDDFT case, however, an overall overestimate of bond lengths in both S_0 to T_1 is observed, which is probably related to the neglect of relativistic effects in these calculations or to possible inaccuracies in the TDDFT geometries resulting from the approximations in the linear response formalism and in the exchange-correlation kernel.

Absorption Spectra. A comparison of calculated and experimental absorption spectra for N926 and N969 are reported in Figures 3 and 4, respectively. The experimental spectra of the two complexes show intense features below 300 nm and less intense features in the range 300−400 nm with tails which extend into the visible region: no absorption is found above 500 nm. It needs to be stressed that within the computational approach used here singlet−triplet excitation energies have zero oscillator strengths because of the neglect of spin−orbit coupling in the TDDFT calculations. To perform a comparison of the experimental and calculated spectra in wavelength regions dominated by low-lying singlet−triplet transitions, we report as insets in Figure 4 and 5 the low-energy portions of the spectra, including the calculated values of singlet−triplet excitations.

The agreement between the calculated and experimental spectra is quite good when the approximations described above are considered. We are indeed able to reproduce the appearance of the main spectral features and their relative intensities, even though the calculated spectra appear to be slightly blue-shifted and for N969 we are partly underestimating the intensity in the 300−350 nm region. For N926, we calculate an intense feature at 255 nm, followed by a shoulder at ∼280 nm, in good agreement with the 268 and 290 nm experimental values. The main peak feature appears to be composed of a series of transitions, dominated by three more intense excitations calculated at 248, 257, and 264 nm (f = 0.41, 0.56 and 0.31), while the 290 nm shoulder is composed of a series of lower intensity transitions in the range 270−300 nm. We notice that in this high-energy region the blue-shift of the calculated spectrum compared to the experimental one is within 0.2 eV, which is a good agreement, considering the rather limited dimensions of the basis set. Inspection of the TDDFT eigenvectors allows us to assign the three main features giving rise to the 268 nm band as overlapping $\pi-\pi^*$ transitions of the bpy and ppy ligands, while the transitions giving rise to the 290 nm shoulder appear to be composed by mixed $\pi-\pi^*$ and metal-to-ligand charge transfer (MLCT) excitations to the ppy-based π^* orbitals, the MLCT character originating from participation of the HOMO−1/HOMO−2 orbitals in the starting states. At longer wavelengths, we calculate three transitions of sizable intensity at 345, 384, and 417 nm (f = 0.13, 0.16, and 0.05), which can be related to the 355, 375 and 417 nm features of the experimental spectrum, see inset of Figure 4. The three transitions have mixed $\pi-\pi^*$ and MLCT character, originating from the HOMO/HOMO−2 set, with the 345 and 417 ones having the ppy π^* LUMO+1/LUMO+2 and the 384 nm one having the bpy π^* LUMO as arriving states. It is interesting to analyze in deeper detail the transitions to the bpy ligand: the lowest-lying singlet−singlet excitation, calculated at 454 nm, is a single HOMO → LUMO transition with negligible intensity (f = 0.0005), while the HOMO−1 → LUMO transition, at 384 nm, is very intense, as discussed above. The intensity difference clearly originates from the different starting orbital because the arriving orbital is in both cases the LUMO. Going back to the electronic structure discussed above, we recall that while the HOMO is an antibonding combination of Ir(t_{2g}) and ppy-(π) orbitals, the HOMO−1/HOMO−2 have Ir(t_{2g}) and bpy-(π) contributions, so that the excited-state resulting from

Table 2. Lowest Singlet−Triplet (S_0-T_1) and Singlet−Singlet (S_0-S_1 and S_0-S_2) Excitation Energies (eV) and Ground-State Energy Differences (ΔS_0, eV) for the N925, N926, and N969 Complexes Calculated in Acetonitrile Solution at the S_0, T_1, and T_2 Optimized Geometries[a]

	N925			N926			N969		
	S_0	T_1	T_2	S_0	T_1	T_2	S_0	T_1	T_2
ΔS_0	0.000	0.067	0.058	0.000	0.124	0.043	0.000	0.146	0.080
S_0-T_1	2.438	2.127	2.353	2.696	2.308	2.474	2.840	2.415	2.648
S_0-S_1	2.472	2.160	2.382	2.801	2.388	2.712	3.181	2.769	3.002
	(0.001)	(0.001)	(0.002)	(0.001)	(0.000)	(0.005)	(0.018)	(0.001)	(0.056)
S_0-S_2	3.069	2.898	2.844	2.985	2.911	2.771	3.186	3.016	3.107
	(0.061)	(0.078)	(0.074)	(0.051)	(0.163)	(0.063)	(0.021)	(0.178)	(0.000)

[a] For S−S excitations, oscillator strengths are also reported.

HOMO−1 to LUMO excitation has a considerable intraligand $\pi-\pi^*$ contribution which, together with the different symmetry of the involved metal orbital, enhances its intensity.

It has to be pointed out that the calculated intensity distribution nicely compares with the experimental one and that in the lower energy range the agreement between the calculated and experimental spectra is within 0.1 eV: this is a general trend which we already observed in Ru(II)−polypyridyl complexes, where low-lying MLCT transitions were described satisfactorily with rather small basis sets, while higher-lying $\pi-\pi^*$ excitations needed higher quality basis sets, including polarization functions, for an improved description.[38e,38h] To gain insight into the origin of the weak band experimentally found at 472 nm, we looked at singlet−triplet excitations, reported in the inset of Figure 4; we can relate the 472 nm band to the presence of two singlet−triplet excitations calculated at 462 and 461 nm. These two transitions have mixed $\pi-\pi^*$ and MLCT character with arriving π^* states localized on the bpy and ppy ligands, respectively. Clearly, we cannot exclude that higher-lying singlet−triplet transitions participating in the overall spectral intensity, even though it is reasonable to assume that their contribution should decrease with decreasing wavelength, that is, in spectral regions where intense singlet−singlet excitations are calculated.

The N969 absorption spectrum is rather similar to that of the N926 complex, and similar bands assignments hold. The high-energy region is dominated by a series of intense overlapping $\pi-\pi^*$ transitions of the bpy and ppy ligands giving rise to an intense band calculated at 255 nm, to be compared to an experimental value of 266 nm, while the intense transitions giving rise to the shoulder calculated at ~280 nm appear to be composed of mixed $\pi-\pi^*$ and MLCT excitations to the ppy-based π^* orbitals. In agreement with the experiment, the shoulder is less pronounced in the N969 case than in the N926 case, while the intensity of the main 266−268 nm band is increased in N969 compared to N926. In the N969 case, we also calculate three quite intense mixed $\pi-\pi^*$ and MLCT transitions at 344, 367, and 390 nm (f = 0.11, 0.17, and 0.04) which can be related to the features experimentally found at 345, 378, and 417 nm, respectively, see inset of Figure 5. The weak band experimentally found at 444 nm is assigned to two almost overlapping singlet−triplet mixed $\pi-\pi^*$ and MLCT excitations calculated at 438 and 437 nm with bpy and ppy π^* arriving states.

It is interesting to point out at this stage that at the calculated S_0 geometries, both N926 and N969 show the lowest singlet−triplet excitations to give rise to almost perfectly degenerate excited states localized on the bpy and ppy ligands. This is in disagreement with the N925 case, where the lowest triplet bpy-based excited-state at the S_0 geometry is calculated at 508 nm, with the ppy-based triplet excited-state being calculated at 451 nm, that is, 0.31 eV higher in energy. We also notice that the calculated values of the lowest singlet−triplet excitations are consistent with the emission blue-shift observed on going from N925 to N926 and N969, with calculated values of 508, 462, and 438 nm, respectively. The calculated values, obtained considering the S_0 optimized geometry, should represent overestimates of the true emission maxima because of the neglect of geometrical relaxation on the excited triplet potential energy surfaces.

Emission. To gain insight into the nature of the excited states involved in the emission process, we repeated the calculation of the lowest singlet−singlet and singlet−triplet excitation energies at the T_1 and T_2 optimized geometries. The energy of the lowest excited states calculated in acetonitrile solution for the investigated complexes are reported in Table 2. It is also interesting to use the singlet−triplet TDDFT excited-state energies calculated at the S_0 and T_1 optimized geometries to draw a schematic representation of the potential energy surfaces involved in the emission of the three complexes.[46] In doing so, one needs to select a distortion coordinate that characterizes the geometrical arrangement of the S_0 and T_1 minima. In particular, we chose to plot the excited-state energies as a function of the $C-C_{(bpy)}$ distances: our choice is dictated by the fact that this parameter shows sizable variations on going from the S_0 to the T_1 minima. The results are reported in Figure 6.

As it can be immediately noticed from Table 2, the emission energies calculated at the S_0, T_1, and T_2 optimized geometries nicely correlate with the experimental data of Table 1. In particular, a considerable blue-shift of the lowest excitation energies is calculated on going from N925 to N926 and N969. Comparison of calculated emission energies with emission spectral maxima is not straightforward, because the emission intensities are determined, for a given couple of electronic states, by vibrational wavefunction overlaps (the Franck−Condon factors) between the excited-state lowest vibrational level and the various vibrational levels of the

(46) De Angelis, F.; Fantacci, S.; Sgamellotti, A.; Cariati, E.; Ugo, R.; Ford, P. C. *Inorg. Chem.* **2006**, *45*, 10576.

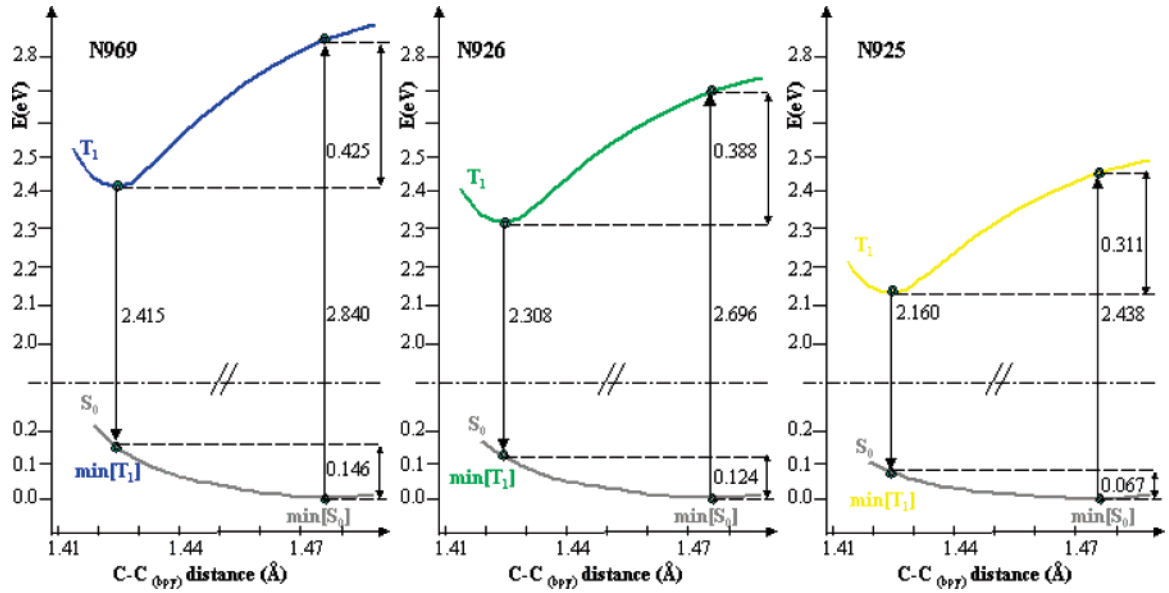

Figure 6. Schematic representation of the calculated potential energy surfaces for the ground state and the lowest triplet excited state of N925, N926, and N969 as a function of the C−$C_{(bpy)}$ bond distance (Å). The zero of the energy (eV) is set in all cases to the ground-state minimum energy.

ground state. We notice that an efficient procedure for the computation of Franck−Condon factors of large molecules in solution, including geometry optimization of the excited states,[47] has been recently achieved.[48] Such a procedure would probably allow us to perform a more direct comparison between calculated and experimental data.

A possible alternative is to compare calculated data with E_{0-0} energies (i.e., the energy differences between the lowest vibrational levels on each potential energy surface) which can be approximately determined by the intersection point between the absorption and emission spectra. In that manner, E_{0-0} values of 2.74 and 2.82 eV are measured for N926 and N969, respectively. The values which better compare with the E_{0-0} values are those calculated for the singlet−triplet excitation energies at the S_0 optimized geometries (2.696 and 2.840 eV for N926 and N969, respectively) with the corresponding values calculated at the relaxed T_1 geometries (2.308 and 2.415 eV for N926 and N969, respectively) being red-shifted compared to both E_{0-0} and the high-energy emission maxima (2.53 and 2.68 eV for N926 and N969, respectively). Moreover, we notice that emission energies calculated at the T_2 optimized structures (2.510 and 2.648 eV, respectively) are calculated, as expected, to lie at higher energies than the corresponding data calculated at the T_1 geometry.

Inspection of the TDDFT eigenvectors allows us to assign the nature of the excited states at the various considered geometries. In particular, our calculations show that at the S_0 and T_1 geometries the lowest triplet excited states of the three complexes are localized on the bpy ligands, while at the T_2 geometry, the lowest triplet excited state is localized on the ppy ligand. We also notice that while for N925 the lowest triplet state at the S_0 and T_1 geometries originates from a single HOMO → LUMO excitation, for N926 and N969 the lowest triplet state has components from both HOMO−2 → LUMO and HOMO → LUMO excitations, with coefficients of 0.34/0.62 and 0.54/−0.48 for N926 and N969, respectively. Therefore the emitting states of all complexes have a mixed MLCT and $\pi-\pi^*$ character, with N926 and N969 showing an increased bpy intraligand $\pi-\pi^*$ contribution compared to N925, resulting from the presence of the HOMO−2 in the emitting state, which has a substantial bpy π character. We also notice that at the T_2 geometries mixing of the HOMO−2/HOMO → LUMO with HOMO → LUMO+1 excitations takes place. The different nature of the triplet and singlet excited states (HOMO−2 → LUMO/HOMO → LUMO and HOMO → LUMO, respectively) gives rise to different energy variations of these states on going from N925 to N926 and N969. When both the S_0 and T_1 geometries are considered, the singlet−singlet excitations almost perfectly follow the HOMO−LUMO gap and, with S_0 as an example, increase by 0.33 and 0.71 eV on going from N925 to N926 and N969, respectively, to be compared with HOMO−LUMO gap increases of 0.31 and 0.74 eV. The singlet−triplet excited states, on the other hand, show a reduced variation and increase by only 0.23 and 0.40 eV (0.18 and 0.29 eV for the T_1 optimized geometries). This different behavior of the singlet and triplet excited states, which is related to their different orbital composition, can be traced back to the different energy variations exhibited by the HOMO and by the HOMO−1/HOMO−2 couple in N926 and N969: while the HOMO is extremely sensitive to fluoride substitution on the ppy ligand, the HOMO−1/HOMO−2 are affected to a minor extent so that the triplet excitations starting from these orbitals are overall less sensitive to functionalization of the ppy ligand. The net results is that the singlet manifold is shifted at higher energy relative to the triplet one in N969 compared to N926 and N925.

(47) Scalmani, G.; Frisch, M. J.; Mennucci, B.; Tomasi, J.; Barone, V. *J. Chem. Phys.* **2006**, *124*, 094107.
(48) Santoro, F.; Improta, R.; Lami, A.; Bloino, J.; Barone, V. *J. Chem. Phys.* **2007**, *126*, 084509.

Radiative and Nonradiative Deactivation. It is interesting to exploit our computational results to rationalize the experimental trend of radiative rate constants, reported in Table 1. Indeed, according to the Einstein theory of spontaneous emission,[22] the radiative rate constant k_r should be proportional to the oscillator strength of the emitting transition and, for a given solvent, increase as the cube of the emission energy, that is, $k_r \propto E^3|M|^2$, where M is the transition dipole moment, the square of which divided by the emitted energy is proportional the oscillator strength. In the cases analyzed here, k_r is found to decrease with increasing emission energy, suggesting a sizable decrease in the oscillator strength of the emitting transition on going from N925 to N926 and N969. Straightforward application of Einstein relation, with consideration of the high-energy edge of the emission spectra as the emitting energy, would imply a decrease of the oscillator strength by 2.2 and 1.9 on going from N925 to N926 and from N926 to N969, respectively. This estimate should be at least qualitatively correct for the three complexes, and the results are rather accurate for N926 and N969, which show a similar shape of the emission spectra. In the case of phosphorescence, the emitting state is of triplet character perturbed by spin−orbit coupling to the singlet manifold and the emission transition dipole moment from the lowest triplet state can be expressed, to first order, as

$$M_{T-S} = \sum_i \{[\langle {}^3\phi_1|H_{SO}|{}^1\phi_i\rangle\langle {}^1\phi_i|M|{}^1\phi_0\rangle]/({}^1E_i - {}^3E_1)\}$$

where ${}^1\phi_i$ and ${}^3\phi_1$ and ${}^1E_i$ and ${}^3E_1$ are the wavefunctions and energies, respectively, of the singlet manifold of excited states and of the lowest triplet excited state, ${}^1\phi_0$ is the singlet ground state wavefunction, H_{SO} is the spin−orbit coupling operator, and M is the electric dipole operator. This very approximate model basically accounts for the fact that the spin−orbit coupled state, which we may identify with the emitting state, borrows its intensity from the manifold of singlet excited states. Considering that the $\langle {}^1\phi_i|M|{}^1\phi_0\rangle$ squared transition dipoles are proportional to the oscillator strength divided by the energy of the considered transition, we can write k_r as[37]

$$k_r \propto ({}^3E_1)^3\{\sum_i [\langle {}^3\phi_1|H_{SO}|{}^1\phi_i\rangle/({}^1E_i - {}^3E_1)]\}^1 f_i/{}^1E_i$$

where ${}^1f_i$ is the oscillator strength of the singlet−singlet excitations, which is calculated together with the transition energies by TDDFT. A simple but again approximate way to estimate $\langle {}^3\phi_1|H_{SO}|{}^1\phi_i\rangle$ matrix elements is to assume a one-center description of the spin−orbit coupling operator, which predicts the coupling matrix element to increase as the content of metal character in ${}^3\phi_1$ increases.[49] In the specific case of MLCT transitions, two restrictions apply for the spin−orbit coupling element to be non-vanishing: (i) the coupled triplet and singlet excited states need to involve the same π^* orbital and (ii) they need to involve metal t_{2g} orbitals with different symmetries. Since the few lowest triplet and singlet excited states are localized on the bpy π^* LUMOs, their coupling is ensured as far as singlet and triplet excited states involve Ir t_{2g} orbitals with different symmetries. On the basis of these considerations, it seems that coupling between S_0-T_1 and S_0-S_2 is responsible of the emission in the investigated complexes, since the S_0-S_2 transition has a substantial oscillator strength and involves the Ir(t_{2g}; $d_{xz}-d_{yz}$)-bpy(π) HOMO−1 starting orbital. On the other hand, because of the vanishing oscillator strength and the involvement of the Ir(t_{2g}; d_{xy})-ppy(π) HOMO as starting orbital, the S_0-S_1 transition is not likely to contribute to the emission intensity.

We can finally estimate the amount of metal character in the lowest singlet−triplet transitions by multiplying the squared coefficient of the TDDFT eigenvector characterizing the excited state[50] by the percentage of metal character in the associated starting orbitals. By doing so and considering the T_1 optimized geometries, we calculate metal contributions to the lowest excited singlet−triplet excitations of 45, 19, and 10% for N925, N926, and N969, respectively. According to this approximation, the increased $\pi-\pi^*$ character calculated for the lowest triplet excited-state in N969 and N926 compared to N925 results in a diminished spin−orbit coupling for this system, thus contributing to the observed reduction of k_r values.

Finally, it is interesting to analyze the measured trend of nonradiative decay rate constants, k_{nr}. As discussed in the Experimental Section, these quantities are found to determine the overall quantum yields by decreasing by approximately a factor 34 on going from N925 to N969. The decrease of k_{nr} with increasing emitted energy is in line with the energy-gap law,[23] which predicts the k_{nr} to decrease exponentially with the emitted energy, and by plotting the ln(k_{nr}) values against the emission maxima energies in Table 1, we effectively find an almost perfectly linear correlation with correlation coefficient 0.996. We may try to rationalize the k_{nr} values in terms of the effect of geometrical relaxation on the excited-state energies. By looking at the data in Table 2 and at Figure 6, we noticed that the geometrical rearrangement taking place upon moving from S_0 to T_1 and T_2 leads only to a modest energy increase, which is at maximum 0.146 eV for the T_1 of N969. On the other hand, relevant changes are observed for the energy of the lowest singlet and triplet excited states on going from S_0 to T_1 and T_2 geometries. The most remarkable changes are calculated for the lowest triplet excited state (Figure 6): on going from S_0 to T_1, we

(49) (a) Azumi, T.; Miki, H. *Top. Curr. Chem.* **1997**, *191*, 1. (b) Solomon, E. I.; Lever, A. B. P. *Inorganic Electronic Structure and Spectroscopy*; John Wiley & Sons: New York, 1999; Vol. I, Chapter 1.

(50) Characterization of the nature of the TDDFT transitions in terms of single-orbital excitations is usually possible, provided one has access to the eigenvectors. The latter are made up of two component vectors, X and Y, related to single-particle excitations and de-excitations, respectively. In G03, however, the program only provides the (dominant) components of the sum vector $X + Y$, and it is thus impossible in principle to separate the interfering excitation and de-excitation components. To the extent, however, that we may reasonably assume that the de-excitation vector Y is small compared to X (it would exactly be zero in the Tamm−Dancoff or single-excitation CI approximation), we may take the square of the $X + Y$ vector components as a qualitative measure of the weight pertaining to the corresponding single excitations. For closed-shell molecules, the G03 TDDFT vectors are actually normalized to 1/2, so we take the double of the squared coefficients.

calculate energy differences in the range −0.311/−0.425 eV, while on going from S_0 to T_2, we found more limited variations in the range of −0.085/−0.222 eV. Comparable energy variations are calculated for the lowest singlet excited states. These data imply that the structural distortions accompanying the formation of the excited states involve much larger energy changes for the lowest excited states than for the ground state, see Figure 6, confirming the reinforcement of $C-C_{(bpy)}/CC_{(ppy)}$ and of metal−ligand interactions in the excited state, as discussed above on the basis of the geometrical parameters variations. This is a new observation since it is generally assumed that metal−ligand bonds and C−C bonds are weaker in the excited state than in the ground state.[8] The reinforced metal−ligand and intraligand interactions do not allow the excited state to perform wide amplitude motions which would allow it to sample nonradiative decay pathways, thus contributing to the reduction of the k_{nr} values. It is also worth stressing that at the S_0 optimized geometries, the triplet excited states localized on the bpy and ppy ligands are almost degenerate in N926 and N969 (within 0.040 and 0.002 eV, respectively), while they are separated by 0.311 eV in the N925 case; this trend is reflected by the LUMO/LUMO+1 energy separation (Figure 3). This degeneracy of the bpy- and ppy-based excited states should help the system to convey the excited-state energy toward the emitting bpy-based state, thus avoiding higher-energy nonradiative decay pathways and ultimately leading to increased quantum yields. We finally notice that nonradiative deactivation pathways involving e_g metal orbitals are quite unlikely to take place for the investigated complexes, since these antibonding states are calculated to lie at very high energy compared to the LUMO.

Summary and Conclusions

In this report, we have demonstrated a strategy for tuning phosphorescence wavelength and enhancing emission quantum yields of iridium cationic complexes by modulating the electronic structure and excited states of the complexes in terms of their lowest occupied and unoccupied orbitals. In particular, we reported the synthesis, electrochemical characterization and photophysical properties of a new cationic Ir(III) complex, [Ir(2,4-difluorophenylpyridine)$_2$(4,4′-dimethylamino-2,2′-bipyridine)](PF_6) (N969), and compared the results with those reported for the analogous [Ir(2-phenylpyridine)$_2$(4,4′-dimethylamino-2,2′-bipyridine)](PF_6) (N926) and for the prototype [Ir(2-phenylpyridine)$_2$(4,4′-*tert*-butyl-2,2′-bipyridine)](PF_6) complex (N925). Electrochemical measurements showed that the ligand-based reduction potentials of N969 and N926 are significantly shifted cathodically compared to that of N925, demonstrating the bipyridine-based LUMO destabilization, which more than offsets the destabilization of the Ir(t_{2g})-ppy(π) HOMO caused by the increased donor capability of the 4,4′-bis(dimethylamino)-2,2′-bipyridine compared to the 4,4′-*tert*-butyl-2,2′-bipyridine ligand, thus ensuring an increase in the HOMO−LUMO gap in N969 compared to those in N926 and N925.

Photophysical data of the three complexes revealed that the high quantum yields afforded by N926 and N969 compared to that of N925 are related to a dramatic decrease in the nonradiative deactivation rate constant, which decreases by a factor 34 as the emission spectrum shifts toward the blue region, reaching a quantum yield value of 85% for N969 with emission edge at 463 nm, in agreement with the energy-gap law. At the same time, the emission lifetimes increase going from N925 to N926 and N969, resulting in an overall reduction of the radiative rate constants by a factor 2, which is suggestive of increased $\pi-\pi^*$ character in the emitting excited states.

The results of DFT and TDDFT calculations on the ground and excited states of the three complexes allowed us to characterize the nature of the excited states involved in the absorption and emission processes. The calculated electronic structure of the three complexes agrees with the electrochemical measurements and highlights, for N926 and N969, the presence of two almost degenerate combinations of Ir(t_{2g}) and π orbitals of the 4,4′-bis(dimethylamino)-2,2′-bipyridine ligand lying close to the HOMO, which are missing in the N925 complex. The LUMO is in all cases a π^* orbital localized on the substituted bipyridine ligand. The HOMO−LUMO gaps increase substantially on going from N925 to N926 and N969, consistent with the emission blue-shift observed experimentally.

For all the investigated complexes, we calculate a reinforcement of carbon−carbon bonds within the bpy and ppy ligands and of metal−ligand interactions upon formation of the lowest triplet excited states, which possibly do not allow the excited-state to perform wide amplitude motions which would allow it to sample nonradiative decay pathways, thus contributing to reduce the k_{nr} values. Most notably, the presence of the HOMO−1/HOMO−2 couple lying close to the HOMO in N926 and N969 has a profound impact on the character of the emitting excited states. Indeed, while for N925, the lowest triplet excited-state corresponds to a single HOMO → LUMO MLCT excitation, for N926 and N969, an appreciable mixing of HOMO−2 → LUMO $\pi-\pi^*$ and HOMO → LUMO MLCT excitations takes place, with the $\pi-\pi^*$ excitation being dominant for N969. The extensive mixing of MLCT and $\pi-\pi^*$ contributions is in agreement with the increase in emission lifetimes observed for N926 and N969 compared to N925.

In conclusion, our results indicate that functionalization of the bpy ligand by electron-donating substituents definitively achieves the objective of shifting the emission energy toward the blue-region of the spectrum, reducing, at the same time, the nonradiative decay pathways. We have shown, however, that for the investigated complexes the destabilization of the functionalized bpy-based π orbitals ultimately leads to a diminished value of the radiative rate constant. The investigated N969 complex, with its 85% quantum yield and emission at 463 nm, is therefore the result of a balanced compromise between the two opposite factors governing the quantum emission efficiency and represents an example of electronic structure-driven tuning of the excited-state properties, thus opening the way to a combined theoretical and experimental strategy for the design of new iridium(III) phosphors with specific target characteristics.

Experimental Section

Computational Details. DFT and TDDFT calculations were performed on N969, N926, and N925 complexes. The geometries of the three complexes were optimized using the BP86 exchange-correlation functional,[51,52] together with TZP (DZP) basis set for Ir (N, C, H), including scalar-relativistic corrections as implemented in the ADF program.[53] Geometry optimizations were performed imposing C_2 symmetry constraints for both the singlet ground state (S_0) and the two lowest triplet states, corresponding to the lowest SCF triplet states obtained by population of the LUMO and LUMO+2 (T_1 and T_2, respectively). At the optimized geometries, we performed TDDFT calculations at the B3LYP/LANL2DZ level of theory[54,55] in acetonitrile solution by means of the PCM solvation model,[56] as implemented in the Gaussian 03 program package.[57] The nonequilibrium implementation of the PCM algorithm was used.[58] For TDDFT calculations, we use the hybrid B3LYP functional, rather than the pure GGA one used for geometry optimizations, because the former has been shown to provide excitation energies in better agreement with experiment than GGA results for transition metal complexes.[38c,38e] Calculation of the lowest 70 singlet−singlet excitations and of the lowest 10 singlet−triplet excitations at the S_0 optimized geometries allowed us to simulate a large (up to 230 nm) portion of the absorption spectrum and to gain insight into the nature of the transitions giving rise to the low-energy spectral region. Calculation of the lowest 10 singlet−singlet and singlet−triplet excitation energies at the T_1 and T_2 optimized geometries, on the other hand, allows us to gain insight into the nature of the lowest emitting states. For G03 TDDFT calculations in solution, no symmetry constraints were imposed. The simulation of the absorption spectra has been performed by a Gaussian convolution with fwhm = 0.4 eV, and the experimental spectra have been rescaled so that the intensity of the experimental and theoretical main feature in the UV match. To check the reliability of the SCF triplet geometries, for N926, we performed TDDFT geometry optimization of the lowest triplet excited state and, for comparison, of the ground state by means of the TURBOMOLE (version 5-7-1) program package.[59] In this stage, we used the same exchange-correlation functional used for ADF calculations, with a default SV(P) basis set and pseudopotential for Ir.

Materials and Methods. The solvents (puriss grade) were purchased from Fluka. 2-Phenylpyridine ligand and hydrated iridium trichloride were used as received from Aldrich and Johnson Matthey, respectively. The ligands, 4,4′-dimetylamino-2,2′-bipyridine[60,61] and 2-(2,4-difluorophenyl)pyridine,[62] and the dichloro-bridged iridium dimers, $[Ir(ppy)_2(Cl)]_2$[6] and $[Ir(dfppy)_2(Cl)]_2$, were synthesized using a reported procedure. UV−vis spectra were recorded in a 1 cm path length quartz cell on a Cary 5 spectrophotometer. Emission spectra were recorded on a Spex Fluorolog 112 using a 90° optical geometry. The emitted light was detected with a Hamamatsu R2658 photomultiplier operated in single-photon-counting mode. The emission spectra were photometrically corrected using a NBS calibrated 200 W tungsten lamp as reference source. The emission lifetimes were measured from a fresh solutions, which were degassed by Ar bubbling for 30 min. Pulsed excitation at 450 nm was provided by a Q-switched, frequency-tripled, Nd:YAG laser pumping an optical parametric oscillator (OPO). The pulse duration was 5 ns, and the repetition rate was 30 Hz. The emission was filtered through a 475 nm cutoff filter and a grating monochromator before being detected by a fast photomultiplier. Voltammetric measurements employed a PC-controlled AutoLab PSTAT10 electrochemical workstation. Cyclic voltammograms (CV) were obtained at a scan rate of 100 mV/s using 0.1 M $TBAPF_6$ as supporting electrolyte in acetonitrile. In all cases, a platinum coil and Ag/AgCl electrode were employed as the counter and reference electrodes, respectively. At the end of the each measurement, the ferrocene/ferrocinium (Fc+/Fc) potential was measured and used as an internal reference. NMR spectra were measured with Bruker ACP-200 spectrometer at 200 MHz, and the reported chemical shifts were referenced to TMS.

The mixed-ligand complexes, $[Ir(2,4\text{-difluorophenylpyridine})_2(4,4'\text{-dimethylamino-2,2'-bipyridine})](PF_6)$ (N969) and $[Ir(2\text{-phenylpyridine})_2(4,4'\text{-dimethylamino-2,2'-bipyridine})](PF_6)$ (N926), were synthesized in a low boiling solvent, dichloromethane, by reaction of the corresponding dichloro-bridged iridium(III) dimer with 4,4′-bis(dimethylamino)-2,2′-bipyridine ligand, yielding 60−70%. In a typical synthesis, the dimeric iridium(III) complex $[Ir(2,4\text{-difluorophenylpyridine})_2(Cl)]_2$ (341 mg, 0.28 mM) was dissolved in 100 mL of dichloromethane solvent under nitrogen. 4,4′-Dimethylamino-2,2′-bipyridine ligand (176 mg, 0.724 mM) was added to this solution. The reaction mixture was refluxed under nitrogen for 5 h; then the solvent dichloromethane was evaporated, and the resulting solid was dissolved in 5 mL of methanol. Ammonium hexafluorophosphate salt solution in methanol was added to this concentrated solution. The resulting precipitate $[Ir(2,4\text{-difluorophenylpyridine})_2(4,4'\text{-dimethylamino-2,2'-bipyridine})](PF_6)$ (N969) was filtered and dried.

$[Ir(2,4\text{-difluorophenylpyridine})_2(4,4'\text{-dimethylamino-2,2'-bipyridine})](PF_6)$ (N969). Yield: 325 mg, 61%. Anal. Calcd for $C_{36}H_{30}F_{10}IrN_6P$: C, 45.05; H, 3.15; N, 8.76. Found: C, 45.69; H, 3.01; N, 9.01. ^1H NMR (CD_3OD): δ 8.38 (2H, d, J= 8.3 Hz), 7.96 (2H, t J= 7.4 Hz), 7.83 (2H, d J= 5.3 Hz), 7.71 (2H, d, J= 3.0 Hz), 7.44 (2H, d, J= 6.7 Hz), 7.19 (2H, dt, J= 8.0 and 2.0 Hz), 6.74 (2H, dd, J= 7.0 and 3.0 Hz), 6.64 (2H, dd, J= 8.0 and 2.0 Hz), 5.76 (2H, dd, J= 8.5 and 3.0 Hz), 3.23 (12H, s).

$[Ir(2\text{-phenylpyridine})_2(4,4'\text{-dimethylamino-2,2'-bipyridine})](PF_6)$ (N926). Anal. Calcd for $C_{36}H_{34}F_6IrN_6P$: C, 48.70; H, 3.86;

(51) Becke, A. D. *Phys. Rev. A* **1988**, *38*, 3098.
(52) Perdew, J. P. *Phys. Rev. B* **1986**, *33*, 8822.
(53) te Velde, G.; Bickelhaupt, M. F.; Baerends, E. J.; Fonseca-Guerra, C.; van Gisbergen, S. J. A.; Snijders, J. G.; Ziegler, T. *J. Comput. Chem.* **2001**, *22*, 931.
(54) Becke, A. D. *J. Chem. Phys.* **1993**, *98*, 5648.
(55) Hay, P. J.; Wadt, W. R. *J. Chem. Phys.* **1985**, *82*, 270.
(56) Miertus, S.; Scrocco, S.; Tomasi, J. *Chem. Phys.* **1981**, *55*, 117.
(57) Frisch, M. J.; Trucks, G. W.; Schlegel, H. B.; Scuseria, G. E.; Robb, M. A.; Cheeseman, J. R.; Montgomery, J. A., Jr.; Vreven, T.; Kudin, K. N.; Burant, J. C.; Millam, J. M.; Iyengar, S. S.; Tomasi, J.; Barone, V.; Mennucci, B.; Cossi, M.; Scalmani, G.; Rega, N.; Petersson, G. A.; Nakatsuji, H.; Hada, M.; Ehara, M.; Toyota, K.; Fukuda, R.; Hasegawa, J.; Ishida, M.; Nakajima, T.; Honda, Y.; Kitao, O.; Nakai, H.; Klene, M.; Li, X.; Knox, J. E.; Hratchian, H. P.; Cross, J. B.; Adamo, C.; Jaramillo, J.; Gomperts, R.; Stratmann, R. E.; Yazyev, O.; Austin, A. J.; Cammi, R.; Pomelli, C.; Ochterski, J. W.; Ayala, P. Y.; Morokuma, K.; Voth, G. A.; Salvador, P.; Dannenberg, J. J.; Zakrzewski, V. G.; Dapprich, S.; Daniels, A. D.; Strain, M. C.; Farkas, O.; Malick, D. K.; Rabuck, A. D.; Raghavachari, K.; Foresman, J. B.; Ortiz, J. V.; Cui, Q.; Baboul, A. G.; Clifford, S. J. *Gaussian 03*, revision B05; Gaussian, Inc.: Pittsburgh, PA, 2003.
(58) Cossi, M.; Barone, V. *J. Chem. Phys.* **2001**, *115*, 4708.
(59) (a) Häser, M.; Ahlrichs, R. *J. Comput. Chem.* **1989**, *10*, 104. (b) Ahlrichs, R.; Bär, M.; Häser, M; Horn, H.; Kölmel, C. *J. Comput. Chem.* **1989**, *162*, 165. (c) Weiss, H.; Ahlrichs, R.; Häser, M. *J. Chem. Phys.* **1993**, *99*, 1262. (d) Bauernschmitt, R.; Ahlrichs, R. *Chem. Phys. Lett.* **1996**, *256*, 454. (e) Bauernschmitt, R.; Ahlrichs, R. *Chem. Phys. Lett.* **1996**, *104*, 9047. (f) Furche, F.; Ahlrichs, A. *J. Chem. Phys.* **2004**, *117*, 7433.
(60) Zakeeruddin, S. M.; Fraser, D. M.; Nazeeruddin, M. K.; Grätzel, M. *J. Electroanal. Chem.* **1992**, *337*, 253.
(61) Maerker, G.; Case, F. H. *J. Am. Chem. Soc.* **1958**, *80*, 2745.
(62) Lohse, O.; Thevenin, P.; Waldvogel, E. *Synlett* **1999**, *1*, 45.

N, 9.47. Found: C, 48.69; H, 4.01; N, 9.84. ^{1}H NMR (CD_3OD): δ 8.14 (2H, d, J= 8.0 Hz), 7.88 (4H, d J= 8.0 Hz), 7.79 (2H, t J= 6.0 Hz), 7.79 (2H, s), 7.69 (2H, d, J= 7.6 Hz), 7.47 (2H, dd, J= 6.0 and 2 Hz), 7.10 (2H, t, J= 6.6 Hz), 7.04 (2H, t, J= 7.6 Hz), 6.68 (2H, dd, J= 6.6 Hz), 6.35 (2H, dd, J= 7.5 Hz).

Acknowledgment. F.D.A. and S.F. thank MIUR for financial support (FIRB 2003: Molecular compounds and hybrid nanostructured materials with resonant and nonresonant optical properties for photonic devices). We acknowledge financial support of this work by the Swiss Federal Office for Energy (OFEN), Philips Technologie GmbH Forschungslaboratorien, Weisshausstr. 2, D-52066 Aachen, Germany. H.J.B. acknowledges the support of the Program "Ramony Cajal" of the Spanish Ministry of Science and Technology.

Supporting Information Available: Optimized geometrical parameters of S_0, T_1, and T_2 of N925, N926, and N969 and low-temperature emission spectra. This material is available free of charge via the Internet at http://pubs.acs.org.

IC700435C